Nano Research
2022, 15(2): 1623–1635
ISSN 1998-0124 CN 11-5974/O4
https://doi.org/10.1007/s12274-021-3711-6

Research Article

Critical adhesion areas of cells on micro-nanopatterns

Shuang Zheng[1], Qiong Liu[1,2], Junhao He[1], Xinlei Wang[1], Kai Ye[1], Xuan Wang[1], Ce Yan[1], Peng Liu[1,3], and Jiandong Ding[1] (✉)

[1] *State Key Laboratory of Molecular Engineering of Polymers, Department of Macromolecular Science, Fudan University, Shanghai 200438, China*
[2] *Navy Characteristic Medical Center, the Second Military Medical University, Shanghai 200433, China*
[3] *College of Bioengineering, Chongqing University, Chongqing 400044, China*

Received: 29 April 2021 / **Revised:** 19 June 2021 / **Accepted:** 24 June 2021

ABSTRACT

Cell adhesion to extracellular matrices (ECM) is critical to physiological and pathological processes as well as biomedical and biotechnological applications. It has been known that a cell can adhere on an adhesive microisland only over a critical size. But no publication has concerned critical adhesion areas of cells on microislands with nanoarray decoration. Herein, we fabricated a series of micro-nanopatterns with different microisland sizes and arginine–glycine–aspartate (RGD) nanospacings on a nonfouling poly(ethylene glycol) background. Besides reproducing that nanospacing of RGD, a ligand of its receptor integrin (a membrane protein), significantly influences specific cell adhesion on bioactive nanoarrays, we confirmed that the concept of critical adhesion area originally suggested in studies of cells on micropatterns was justified also on the micro-nanopatterns, yet the latter exhibited more characteristic behaviors of cell adhesion. We found increased critical adhesion areas of human mesenchymal stem cells (hMSCs) on nanoarrayed microislands with increased RGD nanospacings. However, the numbers of nanodots with respect to the critical adhesion areas were not a constant. A unified interpretation was then put forward after combining nonspecific background adhesion and specific cell adhesion. We further carried out the asymptotic analysis of a series of micro-nanopatterned surfaces to obtain the effective RGD nanospacing on unpatterned free surfaces with densely grafted RGD, which could be estimated nonzero but has never been revealed previously without the assistance of the micro-nanopatterning techniques and the corresponding analysis.

KEYWORDS

biomaterial, surface patterning, cell adhesion, arginine–glycine–aspartate (RGD) nanospacing, poly(ethylene glycol), critical adhesion area

1 Introduction

Cell adhesion to the extracellular matrix (ECM) is key to a series of cellular events that govern the fate of cells, which plays a dominant role in mediating and regulating other cellular processes including but not limited to cell spreading, migration, bidirectional signaling, and wound healing [1, 2]. In other words, cell adhesion to an ECM or a biomimetic material provides further cues that determine cell functionality and fate [3–7], and thus a comprehensive understanding of cell adhesion is of much importance [8–12].

Different from a physiochemical adhesion, cell adhesion is a biological event, which involves outside-in signal transduction, association with the actin cytoskeleton, and assembly of focal adhesion (FA) plagues [13, 14]. In particular, specific cell adhesion is triggered by ligand–receptor binding [15, 16]. The receptors are recruited to the plasma membrane surface, triggering the FA plaques that connect the cytoskeleton to further stabilize the adhesion [17–19]. While the transmembrane protein integrin constitutes the main pertinent receptor family [20–23], the most well-known ligand is a triplet amino acid sequence of arginine–glycine–aspartate (RGD) [24–28].

Thanks to the development of nanopatterning techniques, it has been recognized that RGD nanospacing is critical for specific cell adhesion [29–39], and cells can adhere well only on a surface with a relatively small RGD nanospacing [40–44]. Nevertheless, it does not mean that extremely small nanospacing is necessary for excellent cell adhesion. Even an unpatterned free surface with very dense RGD grafting might not correspond to a "zero" RGD nanospacing, because of not only the sizes of RGD ligands for steric hindrance but also the effective lateral distance of such ligands for collectively transducing signals from outside to inside of a cell. However, no one has revealed the exact effective RGD nanospacing for an unpatterned surface with a dense self-assembled monolayer of RGD ligands. Herein, we will discover this "hidden" value assisted by the micro-nanopatterning techniques and the corresponding analysis based on the concept of critical cell adhesion areas.

Besides nanopatterning, micropatterning is also a unique tool for fundamental studies of interactions between cells and materials [45–54]. In particular, cells were found to adhere on adhesive microislands only over a critical size [55, 56]. Owing to the development of patterning techniques, some micro-nanopatterns have also been fabricated for cell studies [57–61]. However, to the best of our knowledge, the fundamental research of critical adhesion areas has so far been carried out only for

Address correspondence to jding1@fudan.edu.cn

microislands, and there has been no report about critical adhesion area of cells on micro-nanopatterns.

Herein, we addressed some fundamental questions of cell adhesion on biomaterials with nanofeatures and tried to prepare a series of hybrid patterns with different microisland sizes and RGD nanospacings, as schematically presented in Fig. 1(a). We ever defined the term of "critical adhesion area" of individual cells on micropatterned surfaces [56, 62]. Now we would like to examine whether or not the concept of a critical area for adhesion of cells is justified on micro-nanopatterned surfaces, and if yes, whether or not this critical area depends on RGD nanospacing; further if yes, is it possible to explore the underlying critical area of a cell free on an unpatterned surface based on the asymptotic analysis of the critical area on a series of micro-nanopatterns? We hypothesized two characteristic sizes of adhesive microislands for cell adhesion on micro-nanopatterned surfaces, as schematically illustrated in Fig. 1(b). The critical adhesion area denoted as A^* (or A_{C1}) refers to a single cell from non-adhesion to adhesion on microislands, and the critical area of cells from single cell adhesion to multi-cell adhesion is defined as A_{C2}.

As the receptor of the RGD ligand, an integrin molecule is approximately 8–12 nm [63, 64]. If thiol-end RGD agents are linked to a pre-fabricated pattern of fixed gold nanodots with diameters less than 10 nm, the RGD nanoarray can thus well control the eventual integrin array in the cell membrane, and finely regulate cell adhesion on a molecular level. Herein we used a unique micro-nanopatterning technique to enable exploration of the relationship between the critical adhesion area of individual cells and the number of integrin–ligand bindings. Mesenchymal stem cells (MSCs) are an important cell type with rich cell behaviors following cell adhesion on biomaterials [65–70]; in the present study, human MSCs (hMSCs) were employed as the model cells to examine cell adhesion on patterned surfaces.

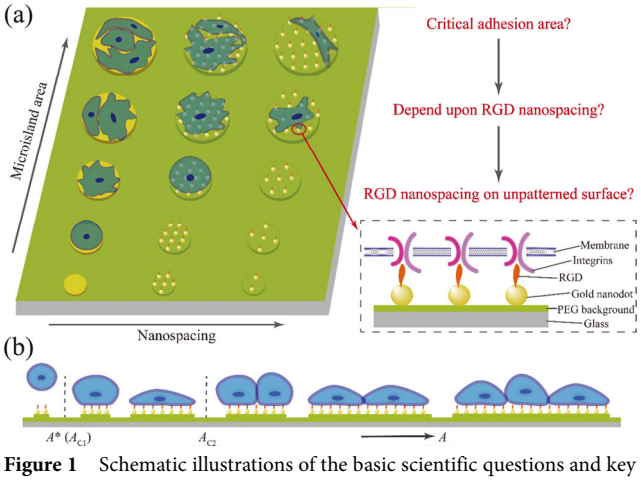

Figure 1 Schematic illustrations of the basic scientific questions and key terms. (a) Micro-nanopatterns and micropatterns of tunable microisland sizes and RGD nanospacings to control cell adhesion. (b) Critical adhesion areas of individual cells on adhesive nanoarrayed microislands with nonfouling background.

2 Experimental

2.1 Fabrication of micro-nanopatterns

The main stages to fabricate the micro-nanopatterns are schematically represented in Fig. 2(c), where we combined block copolymer micelle nanolithography for nanopatterning (Fig. 2(a)), photolithography for micropatterning (Fig. 2(b)), and hydrofluoric acid (HF) etching.

First, block copolymer and gold precursor were dissolved in toluene to form a micelle suspension, which was then dip-coated onto glass to form a self-assembled monolayer. A treatment of oxygen plasma onto the hexagonal micelle array was carried out to remove the block copolymer template and simultaneously reduce the gold acid, resulting in an ordered gold nanoarray (Fig. 2(a)). The preparation process of nano-patterns followed the basic principle of bottom-up. The experimental parameters for the nanopatterning are listed in Table S1 in the Electronic Supplementary Material (ESM).

Then the nanopatterned glass was spin-coated with a photo-resist, covered with a designed micropattern photomask and subsequently exposed to ultraviolet (UV) light. After using HF/NH_4F buffer solution to etch the uncovered region, a micropattern with Au nanodots sparsely arrayed within microislands was generated on the glass. The preparation process of micro-nanopatterns followed the basic principle of combination of bottom-up and top-down (Fig. 2(a)).

We used the same photomask with transparent regions of varied sizes to prepare micropatterns with different microisland areas. The preparation process of micropattern is shown in Fig. 2(b), and the strategy adopted was top-down.

In order to provide a nonfouling background, the glass substrates with all kinds of patterns used in our research were immersed into a silane solution of poly(ethylene glycol) (PEG). Finally, the cyclic peptide c(-RGDfK-)-thiol (f: D-phenylalanine, K: L-lysine; Peptides International), which was originally suggested and synthesized by Kessler group [71, 72], was used as the bridge between gold nanodots on glass slides and integrins at cell surface.

2.2 Cell culture on patterned surfaces and immunofluorescence

hMSCs were seeded on the patterned surfaces for 24 h and then gently rinsed with phosphate buffer saline (PBS) and fixed with 4% paraformaldehyde. After permeabilized with 0.1% Triton X-100, the cells were blocked with 5% bovine serum albumin (BSA) in PBS to avoid nonspecific protein staining. Then, cells were incubated with a primary antibody, mouse monoclonal anti-vinculin primary antibody (Santa Cruz Biotechnology), overnight at 4 °C, followed by triplicate rinse with PBS. Next day, the cells were labeled with an Alexa Fluor 488-conjugated goat anti-mouse second antibody (Invitrogen) at room temperature for 2 h. Then, cells were incubated with phalloidin-TRITC (Sigma) for the staining of filamentous actins (F-actins), and the corresponding dyeing time was about 30 min. At last, cells were incubated with 4′,6-diamidino-2-phenylindole (DAPI, Sigma) for 10 min to show nuclei. For cell counting, the nuclei of hMSCs were labeled with DAPI to reveal the cell number.

The fluorescently stained cells were observed with an inverted fluorescence imaging system (Axio Observer Z1, Zeiss) mounted with a charge-coupled device (CCD, AxioCam MR3, Zeiss).

2.3 Spreading and suspending areas of hMSC cells on an unpatterned free surface

We seeded hMSCs onto RGD-grafted micro-nanopatterns at the density of 4×10^4 cells per well in six-well plates. After 12 h of culture, we randomly selected 6 repeating units from 3 sample surfaces for each kind of nanospacing to observe and analyze hMSCs. For the comparison of characteristic areas of cells on patterned and unpatterned surfaces, we also measured the areas of free spreading cells on an unpatterned surface (A_{spread}) and suspended cells ($A_{suspend}$) using the software Image-J. The

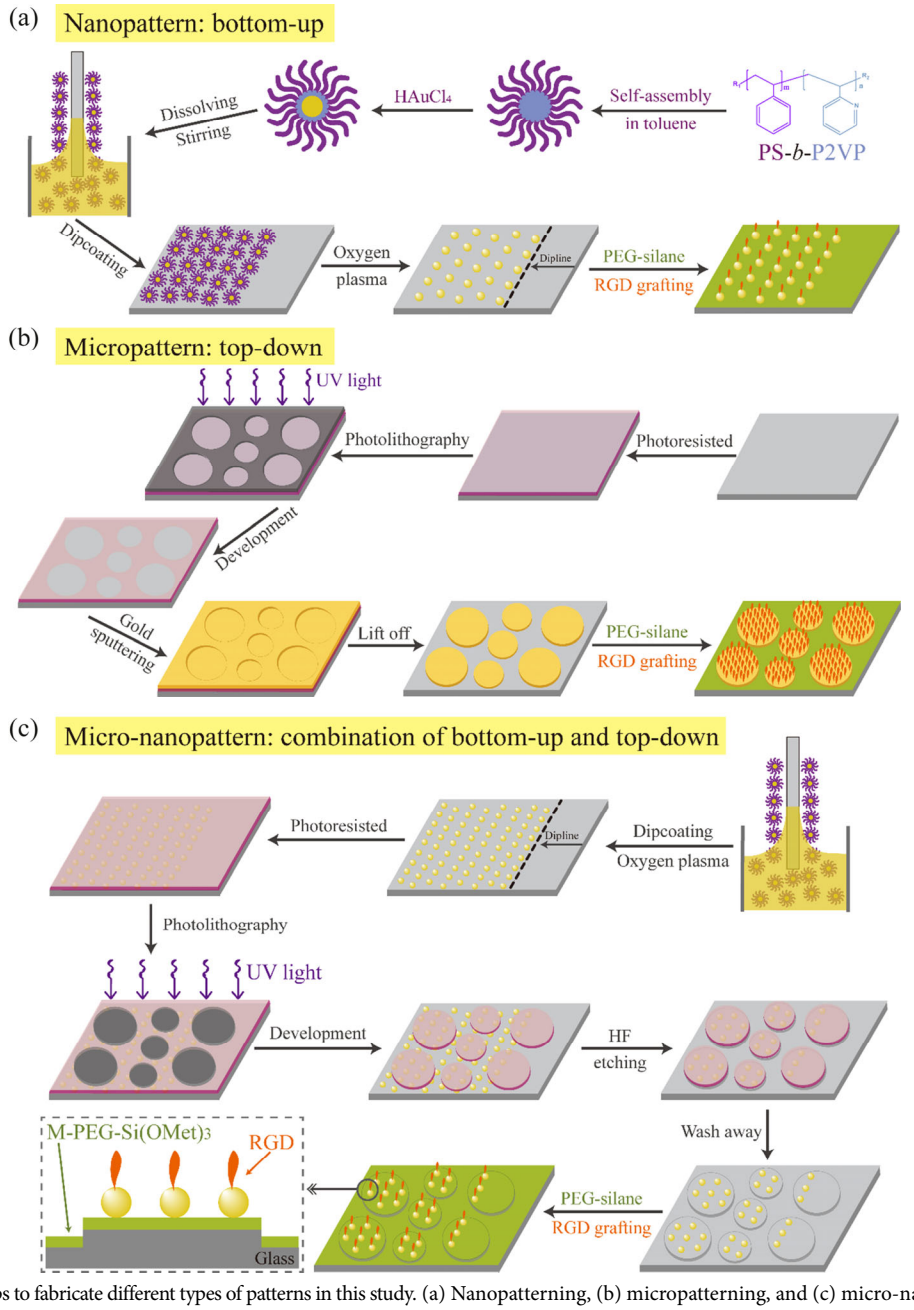

Figure 2 The main steps to fabricate different types of patterns in this study. (a) Nanopatterning, (b) micropatterning, and (c) micro-nanopatterning.

measurement of A_{spread} was based on the bright-field images of hMSCs seeded on tissue culture plates (TCPs) after 8 h. Most cells have spread to common sizes with polygonal morphologies.

2.4 Statistical analysis

All of the data were presented as mean ± standard deviation. Statistical analysis was performed by one-way analysis of variance (ANOVA) to evaluate the difference between indicated groups. A statistical difference was regarded as significant when $p < 0.05$.

3 Results

3.1 Fabrication of micro-nanopatterns

The sizes of the microislands could be adjusted by the sizes of microdomains in a photolithography mask. We designed a mask with round microdomains with diameters from 10 to 80 μm, as shown in Fig. 3(a). Owing to the height difference generated by HF etching between the microislands and their outside regions, the micro-nanopatterns on the glass were visible under an optical microscope (Axiovert 200, Zeiss, Germany) (Fig. 3(b)), which brought us much convenience in the later experiments to judge the success of micro-nanopattern fabrication and also the availability of cell localization.

The size of the gold nanodots and spacing could be adjusted by changing the chain length of the block copolymer, the loading amount of the gold acid in the block copolymer micelles, and the dip-coating velocity, with the corresponding parameters listed in Table S1 in the ESM. We used a field-emission scanning electron microscope (FE-SEM, GEMINI 500, Zeiss, Germany) to observe the resultant micro-nanoarrays. Figure 4(a) shows the FE-SEM images of Au nanoarrays inside some micro-nanoislands and the regions outside the micro-nanoislands where no Au nanodots exist. The average nano-spacings of the ordered nanoarrays varied from 30 to 126 nm in this study. The edges of the micro-nanoislands were sharp and clear, as demonstrated in Fig. 4(b), where the lower right image refers to the edge region of an unnanoarrayed microisland of a micropattern as control. An atomic force microscope

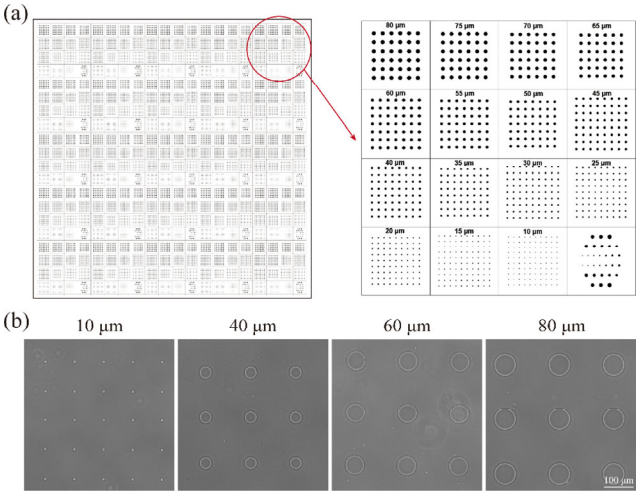

Figure 3 Schematic presentation of the mask and the corresponding experimental results. (a) Left: design of the photomask; right: detailed design of each repeating unit of the photomask. (b) Bright field images showing the microislands prepared by us with various sizes.

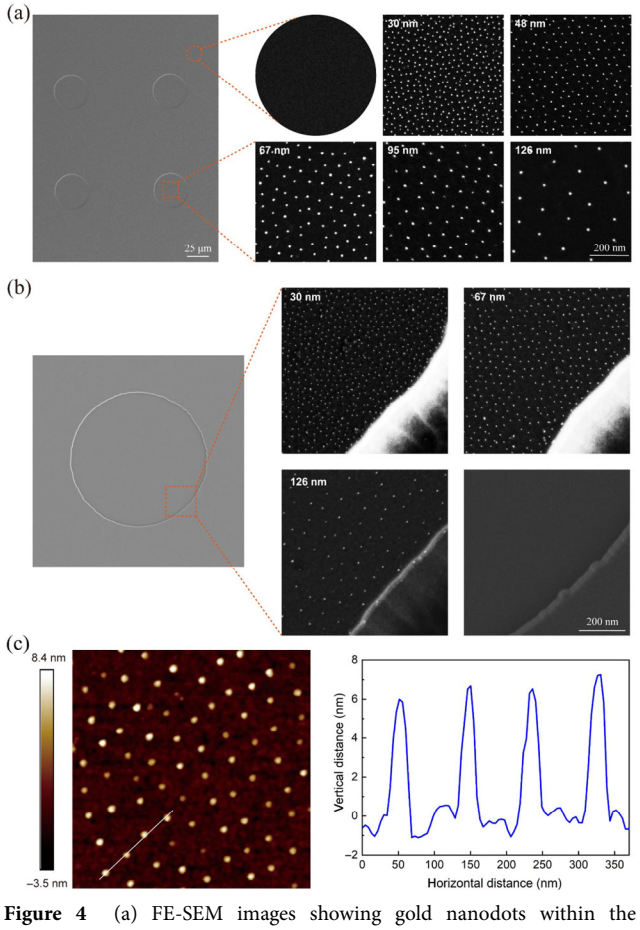

Figure 4 (a) FE-SEM images showing gold nanodots within the microislands (square images in the right column) and the background region outside the gold-nanodot arrayed microislands (round image in the right column). (b) FE-SEM images of a representative microisland (left column), the edges of gold-nanodot arrayed microislands of three micro-nanopatterns corresponding to three different nanospacings (right column), as well as the edge of an unnanoarrayed microisland on a micropattern as control. (c) Microscopic observations of nanopatterns by AFM.

(AFM, Multimode 8, Bruker, USA) was used to determine the sizes of the gold nanodots. A typical AFM image (800 nm × 800 nm) in Fig. 4(c) demonstrated a hexagonal gold nanoarray with the height profile indicating that the sizes of the gold nanodots were as small as 6–8 nm. In addition, the height difference between the micro-nanoisland and the glass substrate can be obtained by scanning large area (50 μm × 50 μm) with AFM, as shown in Fig. S1 in the ESM. Using the AFM analysis software (Nanoscope Analysis) to process the AFM results, the height of the micro-nanoisland can be measured to be about 620 nm. Owing to such a height difference between micro-nanoisland and glass substrate, our prepared micro-nanopatterns were visible. The distribution and shape of micro-nanoislands can be easily seen using the bright field of ordinary microscope, as shown in Fig. 3(b), which provides great convenience for observation and data statistics of subsequent cell experiments.

3.2 The selectively adhesive property of the RGD micro-nanopatterns

To verify that the selectively adhesive RGD micro-nanopatterns constrained the cells within individual microislands on the nonfouling PEG-monolayer-coated substrate, hMSCs were seeded on the micro-nanopatterned surfaces for 24 h; the results are shown in Fig. 5. These fluorescence images demonstrated the excellent localization of cells inside the micro-nanoislands. The dipline in Fig. 5 indicates the boundary of the dip-coated region containing nanopatterns, proving successful fabrication of micro-nanopatterns for selective cell adhesion on the nonfouling background. With the excellent selectively adhesive property of our micro-nanopatterned surfaces, cells rarely passed across the dipline, and primarily occupied the modified region.

In addition, to confirm the long-term resistance of the non-fouling background to cell adhesion, hMSCs were seeded on nanopatterned surfaces with a PEG-coated background for 7 days (Fig. S2 in the ESM). Typical fluorescence images of the counterstained cells on various micro-nanopatterns are shown in Fig. S3 in the ESM. The hMSCs adhered only inside the micro-nanodomain with approximately round shape, wherein the circular micro-nanoislands have diameters of 40 and 80 μm and RGD nanospacings of 30 and 126 nm. We can see distinct adherent difference between microisland diameters and nanospacings, and the details are shown in the ESM. It is obvious that cells adhered better and more on micro-nanoislands with a large diameter and small nanospacing. However, it is not easy to expect the relationship between micro-nanoisland size and RGD nanospacing around the critical adhesion areas.

It is worthy of noting that an excessive amount of the RGD reagent was casted onto the gold nanodot arrayed surfaces and thus one gold nanodot could link to one or a few RGD ligands.

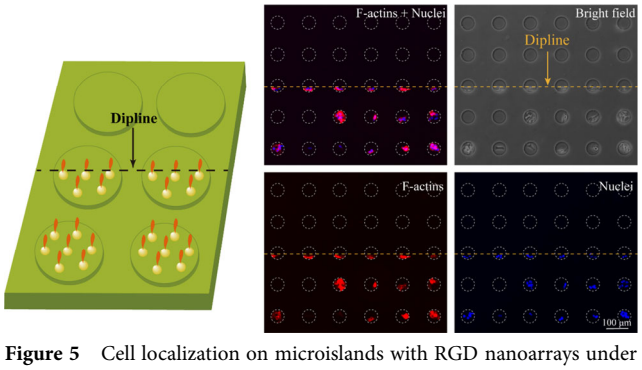

Figure 5 Cell localization on microislands with RGD nanoarrays under a PEG background. The left image illustrates the dipline and nanoarrayed micro-nanopattern regions. Those on the right are fluorescence images showing that hMSCs adhered near the dipline, and the dashed circles represent the contour of the microislands with a diameter of 60 μm. The dipline indicates the boundary of the dip-coated region, and the optical micrographs with cells illustrated well the successful fabrication of micro-nanopatterns for cell studies. F-actins were stained in red fluorescence using phalloidin and cell nuclei were stained in blue using DAPI.

Nevertheless, the first RGD–integrin bioconjugate would sterically hinder the binding of the remaining RGD ligands to its receptor, if the sizes of the gold nanodots are less than 10 nm, the size of an integrin. So, the nanospacing of the initial gold nanoarray on the substrate can well determine that of the eventual integrin nanoarray in the cell membrane.

3.3 Spreading and suspending areas of hMSC cells on an unpatterned free surface

To roughly estimate the adhesion extents of hMSCs on patterned surfaces, we measured the area of free spreading cells on an unpatterned surface (A_{spread}) and suspended cells ($A_{suspend}$) using the software Image-J. The statistical result was A_{spread} = 1492 ± 62 μm^2. The $A_{suspend}$ was analyzed according to bright-field images with clear morphology boundary, and had a value of 223 ± 8 μm^2. At least 100 spreading cells and suspended cells were randomly selected to determine the average area for each sample.

3.4 Experimental method to determine the critical adhesion area of cells on micropatterns and micro-nanopatterns

Figure 6(a) first demonstrates single cells followed by multiple cells adhering on both gold-sprayed micropatterned (upper panel) and 67 nm nanospaced micro-nanopatterned (lower panel) surfaces, where the dashed circles indicate the contours of the underlying RGD-grafted microislands and micro-nanoislands. With the enlargement of the microislands, cells exhibited a transition from non-adhesion to adhesion, and the transition values differed between the micropatterns and micro-nanopatterns. It implies the existence of a "critical adhesion area" on adhesive microislands of varied sizes and its dependence on RGD nanospacing.

A micro/nanoisland with either one cell or multiple cells is regarded as "occupied." The occupation fraction $f_{N>0}$ (the subscript N indicates cell number) is defined as the percentage of occupied islands among all statistical microisland units. Figure 6(b) demonstrates the determination of the characteristic areas such as A^* (the critical area from nonadhesion to survival) and A_{C2} (the critical area from single cell adhesion to multi-cell adhesion). More data are shown in Figs. S4–S6 in the ESM.

When a microisland was sufficiently small, the probability of cells to adhere on the nanoarrayed microisland was almost zero. As the adhesive area increased, $f_{N>0}$ gradually increased from zero to unity, which demonstrated a transition from "non-adhesive" to "adhesive" nanoarrayed microisland, or implied a switch from eventual cell "apoptosis" to "survival" (Fig. S5 in the ESM). The cross point of two tangential lines was employed to determine the critical point. In this way, we obtained the critical area from apoptosis to survival A^*, similar to the determination of critical micelle concentration (CMC) from the optical density (OD) versus amphiphile concentration in studies of the micellization transition of amphiphiles in a selective solvent [73, 74]. Similarly, we defined a microisland with at least two cells as "multioccupied." The fraction of multi-occupation $f_{N>1}$ denotes the percentage of multi-occupied islands, and the curve of $f_{N>1}$ versus adhesive area also exhibited a similar transition resembling CMC.

To verify the possible influence of the critical adhesion areas by adjusting the cell seeding density, we seeded hMSCs

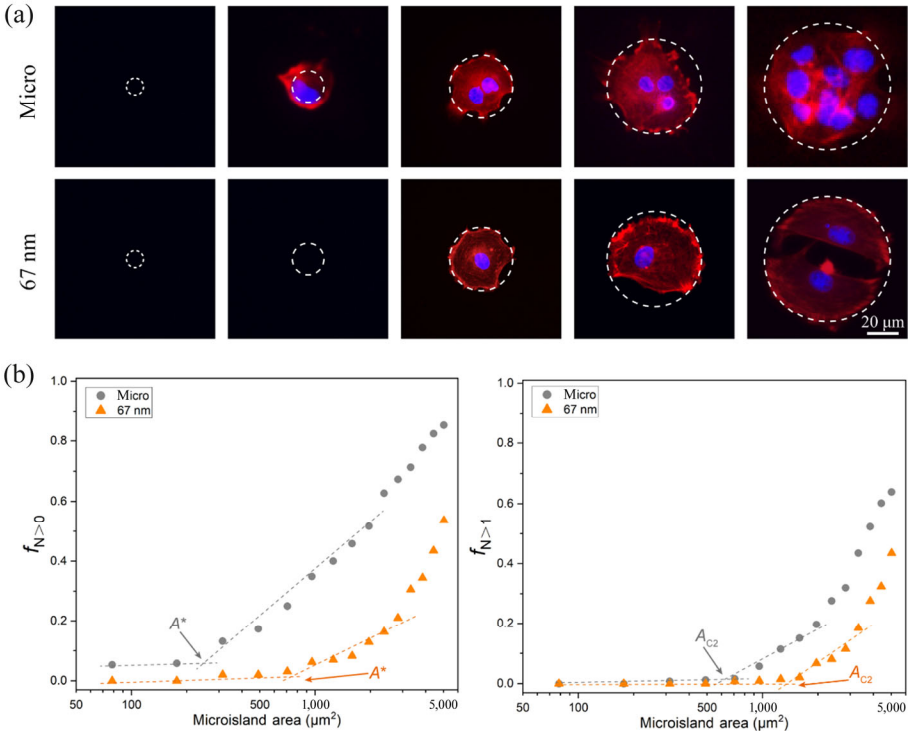

Figure 6 Critical adhesion areas of cells obtained by observation of cell numbers on microislands with increased sizes. (a) The relationship between cell numbers and the sizes of microislands together with nanospacings of micro-nanoislands. Fluorescence micrographs of hMSCs adhering on gold-sprayed microislands grafted with RGD ligands (upper panel) and on micro-nanopatterns with RGD ligands grafted on hexagonally arranged arrays of gold nanodots that were 67 nm nanospaced (lower panel). The F-actins were stained in red, and the nuclei were stained in blue. The number of nuclei indicates that of adherent cells on each micro/micro-nanoisland within the contour marked by the dashed circles. (b) The experimental approach to determine critical adhesion areas of cells on micro-nanopatterns with increasing microisland sizes. Left: fraction of cellular occupation per microisland ($f_{N>0}$) on mere micropatterns (gray circles) and on 67 nm nanospaced micro-nanopatterns (orange triangles). Right: fraction of occupation of multiple cells per microisland ($f_{N>1}$) on micropatterns and on 67 nm nanospaced micro-nanopatterns. The critical areas A^* and A_{c2} are from the crosspoints between the corresponding two marked asymptote lines of $f_{N>0}$ and $f_{N>1}$, respectively.

onto RGD-grafted nanoarrayed microislands at three densities. The results in Fig. S6 in the ESM indicated that A^* did not significantly change with cell seeding density.

We found that A^* and A_{C2} varied from micropattern to micro-nanopatterns, and increased with RGD nanospacing. According to Fig. 7, the results of the 3 groups with nanospacings smaller than 70 nm, which is a crucial nanospacing value for cell adhesion as studied previously [40, 41], exhibited good linear relationship.

It is not hard to understand that the micropatterned surface cannot be simply considered as of zero RGD nanospacing or in a general sense the effective nanospacing for cell adhesion on an unpatterned surface even with densely grafted RGD ligands is not necessarily zero. However, researchers have neither predicted such an effective RGD nanospacing previously nor suggested a feasible experimental method. With our unique micro-nanopatterning technique, we can control cell localization and spreading in a fine manner and further calculate the corresponding areas, which implied a mathematical trend. In order to calculate the effective nanospacing, we made fitting of the data for A^* and A_{C2} with respect to nanospacings < 70 nm in Fig. 7. The intersection of the two lines corresponds to the minimal effective nanospacing, wherein A^* corresponds to 19.14 nm (Fig. 7(a)) and A_{C2} corresponds to 19.12 nm (Fig. 7(b)).

3.5 The relationship between adherent cell area and nanospacing together with micro-nanoisland size

Typical fluorescence images of single hMSCs on micro-nanopatterns with different nanospacings of nanoarrayed microislands are shown in Fig. 8(a). The hMSCs on micro-nanopatterns with nanospacing smaller than 70 nm adhered well inside the microislands. When the nanospacing of micro-nanopatterns exceeds 70 nm, cells did not cover the entire microisland.

Then, we analyzed over 90 cells from three samples for each group of micro-nanoislands and nanospacings, and only single cells inside an individual micro-nanodomain were selected as statistical targets. The left in Fig. 8(b) is a three-dimensional (3D) image showing average single cell area as functions of microisland size and RGD nanospacing. Then, the data were

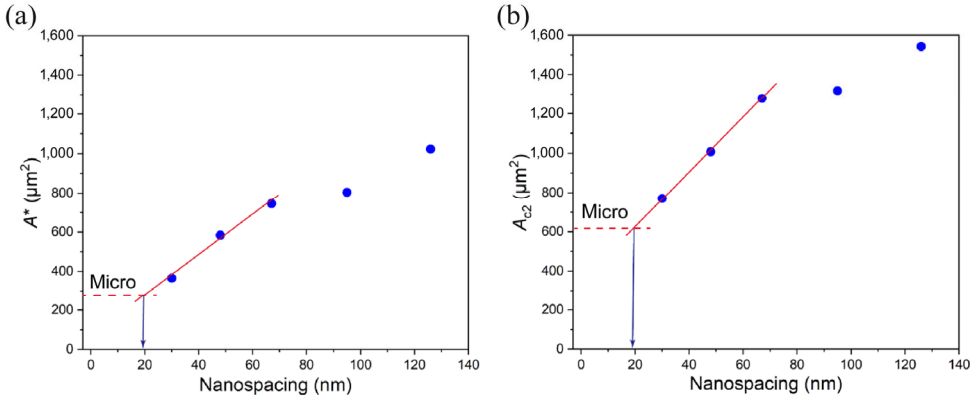

Figure 7 Dependence of the critical adhesion area on RGD nanospacing on a series of micro-nanopatterns and the asymptotic analysis of the effective RGD nanospacing on a free surface without patterns. A^* (a) and A_{c2} (b) increased with RGD nanospacing. The partial linear fitting curves for nanospacing < 70 nm of A^* and A_{c2} were used to deduce the effective RGD nanospacing of an unpatterned surface with densely grafted RGD ligands, resulting in $A^* \approx 19.14$ nm and $A_{c2} \approx 19.12$ nm.

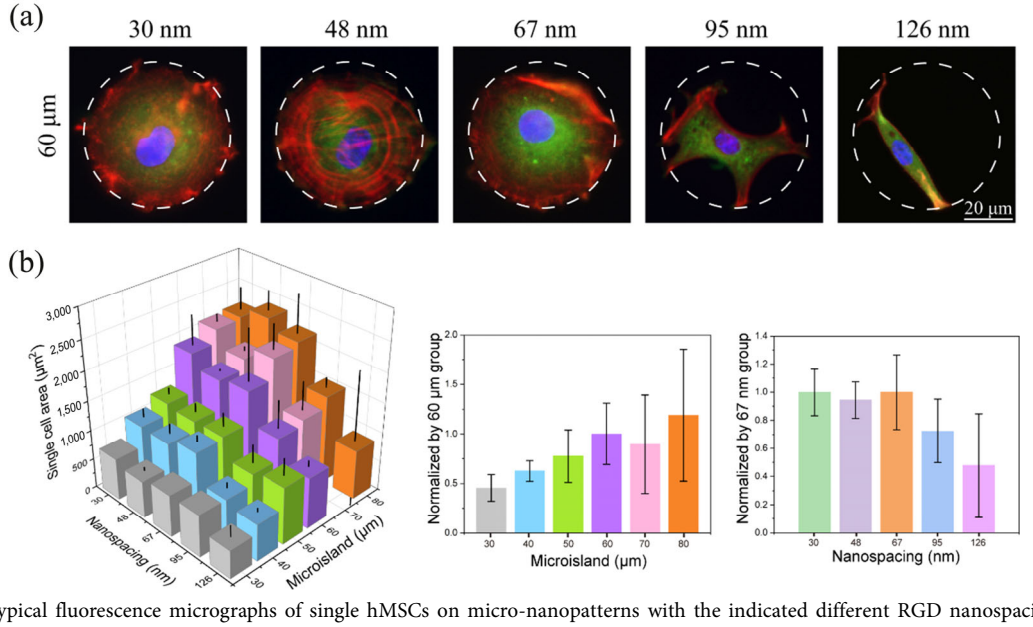

Figure 8 (a) Typical fluorescence micrographs of single hMSCs on micro-nanopatterns with the indicated different RGD nanospacings. Herein, 60 μm-diameter microislands were used as demonstration. The adherent cells were stained to show F-actins in red, vinculin in green, and nuclei in blue. (b) Spreading areas of single cells on micro-nanopatterns. Left: 3D image showing average single cell area as functions of microisland size and nanospacing. Middle: average single cell area as a function of microisland size normalized to the 60 μm-diameter group, $p = 3 \times 10^{-5}$, $n = 15$. Right: average single cell area as a function of nanospacing normalized to the 67 nm nanospacing group, $p = 1 \times 10^{-7}$, $n = 18$. The global test among all of the groups was analyzed from ANOVA.

grouped by the diameter of microislands and normalized to the 60 μm-diameter group, as shown in the middle of Fig. 8(b). Regardless of the nanospacing, the average single cell area showed an overall increasing trend with the micro-nanoisland diameter.

The right in Fig. 8(b) is grouped by nanospacing and normalized to the 67 nm nanospacing group. Regardless of the micro-nanoisland size, the average single cell area showed an overall declining trend with the increase of the nanospacing, and this trend became much apparent when nanospacings were over 70 nm. The *p* values from global tests among all of the groups analyzed from one-way ANOVA are listed in Tables S2 and S3 in the ESM.

According to the above experimental results on micro-nanopatterns, we confirmed that with the increase of microisland areas, the cells would have more space to spread. Meanwhile, the spread of cells was also limited by the nanospacing, where the spread of cells was still insufficient with the large nanospacing over 70 nm.

3.6 The density of adherent cells as functions of RGD nanospacing and microisland size

Besides average area of single cells, the resultant density of the adherent cells (cell number per 1,000 μm^2) is also a crucial parameter to characterize the extent of cell adhesion on a substrate. We summarized the detailed data about adhesive cell density versus microisland size and nanospacing in Fig. S7(a) in the ESM. Then, the data were grouped by the diameter of microisland and normalized to the 60 μm-diameter group, shown in the left of Fig. S7(b) in the ESM. Regardless of the nanospacing, with the micro-nanoisland diameter increasing, the adhesive cell density exhibited a tendency of increase. The right of Fig. S7(b) in the ESM shows the data grouped by nanospacing and normalized to the 67 nm nanospacing group. Regardless of the micro-nanoisland size, the cell density exhibited a trend of decrease with the increase of RGD nanospacing. The *p*-values obtained from one-way ANOVA listed in Tables S4 and S5 in the ESM. The detailed comparison of cell areas and cell numbers on 40 μm-diameter and 80 μm-diameter micro-nanoislands (Fig. S8 in the ESM) further strengthens the above trends of cell parameters with RGD nanospacing on the substrate.

3.7 Calculation of critical number of integrin–ligand binding (*N**)

Then we tried to figure out a unified interpretation of the nanospacing-dependent critical adhesion areas of individual cells on micro-nanopatterns. As is known, cell adhesion to ECM is primarily mediated by the integrin family of heterodimeric receptors [21, 63, 64]. The integrin-mediated focal adhesion is also the site at which contractile forces produced inside the cell are exerted onto the substratum, and consequently their distribution indicates the size and shape of the cell. With the help of our micro-nanopatterning technique and the controlled small size of Au nanodots, we can achieve a one-to-one binding between an integrin and an RGD-grafted Au nanodot. Considering the importance of integrin binding [75–77], we define the number of binding between integrins and ligands as *N*, and thus the critical number of integrin–ligand binding as *N**. We calculated the total number of nanodots N_{total} (Fig. S9 in the ESM) using the equations derived in Fig. 9(a) and in the ESM, which is related to nanospacing and *A**. The resultant *N** as a function of nanospacing is shown in the Fig. 9(b). It can be seen that *N** decreased with the increase of nanospacing rather than keeping as a constant, which was, to be honest, not quite as initially expected. Therefore, we carried out further analysis.

3.8 Calculation of reduced adhesion force of single cells on micro-nanopatterns

We eventually found a unified interpretation after addition of a parameter related to non-specific cell adhesion besides the integrin-mediated specific adhesion. When we looked into the relationship between critical adhesion area and the inverse of nanospacing, we realized that the intercept of the linear fitting of the 3 groups over 70 nm revealed the area of background adhesion of cells, which was about 1,270 μm^2 (Fig. 10(a)). This reciprocal method was employed from the data treatment of molecular simulations to examine the finite size effect with a given simulated box size and calculate the theoretical value under an infinite system with 1/(box size) → 0 [78]. In our opinion, this area has a physical meaning of the theoretical adhesion area of a free cell on a non-fouling background, where nanospacing is infinite because of no ligand binding between the cell and ECM at this point. The theoretical free adhesion area was smaller than the unrestricted spreading area (A_{spread}) of 1,492 μm^2, and reasonably larger than the projected area of a suspending cell of an hMSC ($A_{suspend}$) of 223 μm^2. Unlike specific adhesion binding to receptors on the membrane, non-specific background adhesion always exists and might be correlated with the adhesion area. Thus, this kind of non-specific background adhesion is defined as "background adhesion" in this article.

We reasonably inferred that cell adhesion force was provided

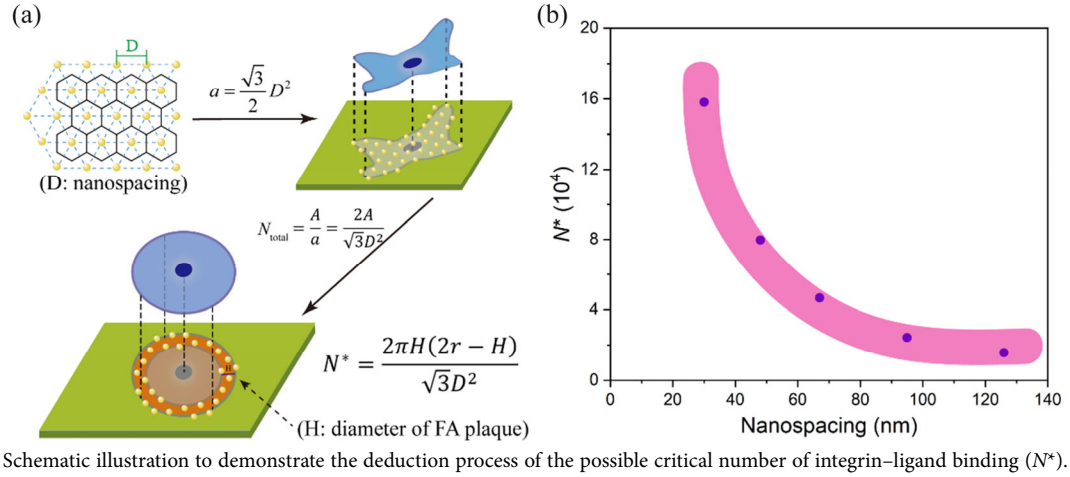

Figure 9 (a) Schematic illustration to demonstrate the deduction process of the possible critical number of integrin–ligand binding (*N**). (b) The curve of *N** versus nanospacing based on experimental results.

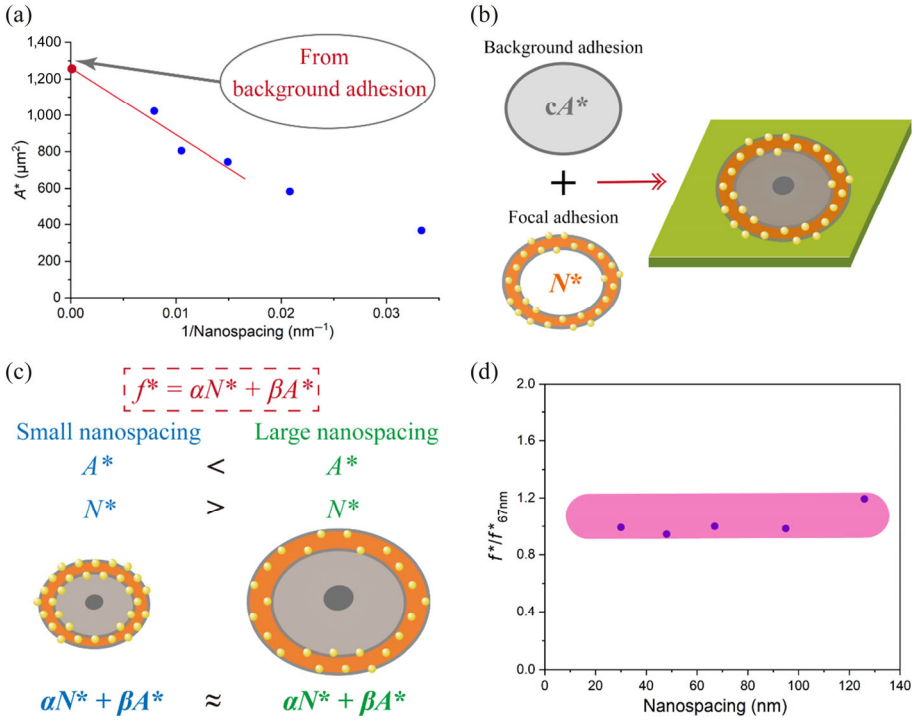

Figure 10 (a) Relationship between critical adhesion area and the inverse of RGD nanospacing, where the intercept of the linear fitting curve revealed a characteristic area related to background adhesion of cells that was about 1,270 μm^2. (b) Definition and schematic illustration of f^* which indicates the adhesion force of cells. (c) Schematic of adhesion force f on microislands with nanoarrays of small and large nanospacings. Herein, α and β denote the coefficients about specific cell adhesion triggered by affective RGD–integrin bioconjugates and nonspecific cell adhesion contributed by background adhesion, respectively. (d) The calculated f^* as a function of RGD nanospacing normalized to f^* at 67 nm nanospacing.

by two parts: One was through the integrin–ligand binding, and the other was through the background adhesion, wherein the role of background adhesion might be proportional to the adhesion area, as shown in Fig. 10(b). Based on the concept of background adhesion, the phenomenological adhesion forces (f^*) with small and large nanospacings are shown in Fig. 10(c) in a comparative way, where we suggest that the f^* of the same cell type with different nanospacings be roughly the same. Cells in the case of small RGD nanospacing had a small critical adhesion area (A^*) which can offer relatively weak background adhesion; meanwhile, the nanodot density was high, which could lead to more integrin–ligand bindings.

Therefore, we put forward a formula to illustrate the relationship between adhesion force, integrin–ligand binding and background adhesion as $f^* = \alpha N^* + \beta A^*$, or $N^* = f^*/\alpha - \beta/\alpha A^*$. The fitting between N^* and A^* is demonstrated in Fig. S10(a) in the ESM. The source of the coefficient of the calculation formula related to background adhesion, which is as a function of critical adhesion area. The forces normalized to the 67 nm nanospacing group are presented in Fig. 10(d). The corresponding f^*/f^*_{67nm} values of the 5 different nanospacings are substantially consistent with each other. More analysis is shown in Fig. S10(b) in the ESM.

3.9 Single cells on micro-nanoislands and microislands

To help better understand the adhesion-related concept, we comparatively observed single cells on micro-nanoislands and microislands. According to the critical adhesion area of micro-nanopatterns with nanospacings of 30, 67, and 126 nm, we calculated the corresponding theoretical cell diameters as 22, 31, and 36 μm, respectively, and the closest diameters of the nanoarrayed microislands larger than the theoretical values among prepared micro-nanopatterns are 25, 30, and 40 μm, respectively. Some typical cell morphology on these nanoarrayed microislands is demonstrated in Fig. S11 in the ESM, where hMSCs were stained to show F-actin in red, vinculin in green, and nucleus in blue. Most of single cells on a 30 nm nanospaced micro-nanoisland with 25 μm-diameter protruded out of the microisland range, and the microisland of 25 μm was not much larger than the suspension area of an hMSC with $A_{suspend}$ about 223 μm^2. In contrast, cells on a 67 nm nanospaced micro-nanoisland with 30 μm-diameter substantially covered the whole microisland, and cells on a 126 nm nanospaced micro-nanoisland with 40 μm-diameter usually cannot occupy the whole microisland.

We further looked into this concept in three dimensions. Two typical 3D reconstruction images of single cells on small (upper panel) and large (lower panel) microislands are shown in Fig. S12 in the ESM. The top view illustrates that the single cell on the small microisland protruded out of the microisland range, while the single cell on the large microisland cannot cover the whole microisland. The side view and 3D reconstruction showed the Z-dimension and indicated that the cell on the large microisland spread better with flat morphology while the cell on the small microisland had an upright appearance.

We turned to examine single hMSC cells on micro-nanoislands of varied nanospacings and varied microisland diameters. Very few cells could adhere on 30 nm nanospaced micro-nanoisland with 10 μm-diameter and these few cells exhibited a projected area significantly larger than the area of the microisland (Fig. S13(a) in the ESM). This is reasonable, because the area of a micro-nanoisland with 10 μm-diameter was even far smaller than the suspension area of hMSCs ($A_{suspend}$ of 223 μm^2). Figure S13(b) in the ESM shows cells on 126 nm nanospaced micro-nanoisland with diameters of 45, 65, and 80 μm; the cells generally did not cover the entire micro-nanoislands and were rarely round-shaped. The above observations illustrated different 3D behaviors of cells on adhesive nanoarrayed microislands of varied RGD nanospacings and microisland sizes. The different 3D shapes of cells were

reported by Guo et al. when they examined cell volumes on relatively stiff and soft matrix without surface patterning [79]; they indicated that less spread rose to larger heights and even the cell volume and stiffness could be changed.

4 Discussion

4.1 Relationship between cell–ECM contact area and projected cell area on micropatterns in the literature & RGD nanospacing dependent critical adhesion areas of cells on micro-nanopatterns in the present study

The pioneering work to design patterned surfaces to control cell adhesion was reported in the journal *Science* by Chen et al. in 1997 [55]. Their micropatterns were prepared with microcontact printing of a hydrophobic chemical with a thiol end group on a gold surface, followed by formation of a self-assembled monolayer of a nonfouling chemical. The ECM protein fibronectin (FN) with amphiphilicity was then adsorbed onto the hydrophobic microislands, and a flat micropattern with cell-adhesion contrast between FN microislands and nonfouling background was eventually established. For those microarrays of altered nonfouling distances between the nearest neighbor adhesive microislands of subcellular sizes, they defined the summation of the areas of the microislands under a cell as "cell–ECM contact area," which could be smaller than projected cell area. It is interesting that "DNA synthesis scaled directly with projected cell area and not with cell–ECM contact area" [55]. Such a view point that the project area is, to a certain extent, more important that the ECM contact area, was strengthened by their paper in 2003 [80].

Based on microislands with cell sizes, the paper published in *Science* in 1997 also indicates "capillary endothelial cells were switched from growth to apoptosis by using micropatterned substrates that contained extracellular matrix-coated adhesive islands of decreasing size to progressively restrict cell extension" [55]. The term of critical cell adhesion area was suggested by Ding's group in 2011 [56]. Besides the critical adhesion area from apoptosis to survival denoted as A^* or A_{c1}, our group also defined the critical area from adhesion of a single cell to adhesion of multiple cells (A_{c2}), and established the way to determine them experimentally. In the present study, we justify the concept of critical cell adhesion area on micro-nanopatterns for the first time.

Since the projected area of a cell plays more important role in cell adhesion as revealed by Chen et al. using microarrays of subcellular microislands [55, 80], it seems possible that the critical adhesion area might be independent upon RGD nanospacing. However, our series of experiments on micro-nanopatterns in the present study definitely indicate the dependence of critical adhesion area of cells on RGD nanospacing. It has been known from the studies of nanopatterns [30, 35, 40, 41, 43, 44] and also confirmed in our micro-nanopatterns (Fig. 8) that a cell on a microregion without significant constraint always spreads less on RGD nanoarrays with large nanospacings, in particular, > 70 nm. However, the critical adhesion areas of cells on micro-nanopatterns with given RGD nanospacings exhibited a significant increase with the nanospacing (Fig. 6). This is not unreasonable because a large RGD nanospacing has less adhesion capacity and thus a larger cell spreading area is required to achieve a critical cell adhesion. These results also illustrate that the relationship of cell–ECM contact area and projected cell area on micropatterns of subcellular resolution cannot be simply extended to those on micro-nanopatterns with very small nanodots reflecting the molecular level.

It is interesting that the total number of gold nanodots is not a constant among the nanoarrayed microislands with respect to critical cell adhesion under different RGD nanospacings, as seen in Fig. 9(b). We further combine the specific adhesion triggered via RGD–integrin bioconjugation and the nonspecific background to unify the total adhesion extent in the cases of critical cell adhesion on different series of micro-nanopatterns with varied nanospacings, as seen in Fig. 10.

4.2 The deduction of the minimal effective nanospacing

It is amazing that our series of critical adhesion areas of mammal cells on micro-nanopatterns can reveal the minimal effective nanospacing on microislands or unpatterned free surface with extremely dense RGD grafting, which is otherwise very hard to be investigated and so far, has never been pointed out. From our experimental results, we found that both A^* and A_{c2} varied from micropattern to micro-nanopatterns, and increased with RGD nanospacing. Assistant by the micro-nanopatterning techniques and our analysis based on the critical cell adhesion areas under given RGD nanospacings, we deduced that the working nanospacing on micropatterns or free surfaces with extremely dense RGD grafting might be about 19 nm, as shown in Fig. 7. The results of the effective nanospacings from the two series in Fig. 7 are consistent with each other very well.

Lehnert et al. once reported that a good cell spreading extent reached only at a surface coating above 15% by using regular micropatterns of ECM protein dots of defined sizes separated by nonadhesive regions [75]. Inspired by their work, we also calculated the coverage of gold nanodots on the nanopatterns. For the group of smallest nanospacing (in the 30 nm nanospacing group) with best cell adhesion in our study, the calculated gold coverage was 6.4% upon assumption of a hexagonal arrangement of 8 nm nanodots. Even this maximum ECM coverage in our studies based on nanopatterns is significantly less than the transition value of 15% based on their micropatterns, which implies that all of ligand sites on micropatterns are not effective to cell adhesion or most of ligand sites are not eventually involved in an effective cell adhesion. It is interesting that the effective nanospacing (19 nm) revealed in our studies corresponds to a nanodot coverage of 16.1%, close to their ECM coverage of 15% on arrays of microislands with subcellular sizes.

4.3 The underlying RGD nanospacings to regulate cell adhesion

Now, we summarize the underlying effective RGD nanospacing of cell adhesion in Fig. 11. The size of RGD is regarded as 1–2 nm [81], assuming that the RGD reagent can be tightly packed and grafted onto a gold surface. Since an integrin is a protein molecule much larger than the RGD ligand [82, 83], after one-to-one bioconjugating between an integrin and the ligand(s) at one small nanodot, some RGDs grafted on gold nanodots might be redundant for a static adhesion. So, at this time, the minimal effective nanospacing follows the integrin size of 8–12 nm.

Integrins connect FA complex inside the membrane and interact with cytoskeletal components to trigger focal adhesion that involves structural proteins such as vinculin, talin and α-actinin, and signaling molecules including FAK and paxillin. Combination of the dimension of a FA complex and the projected size of a pair of α-actinin within the cell as shown in the upper right of Fig. 11, the feature size along the material surface might be about 15 to 30 nm, which primarily interprets the minimal effective RGD nanospacing for an unpatterned

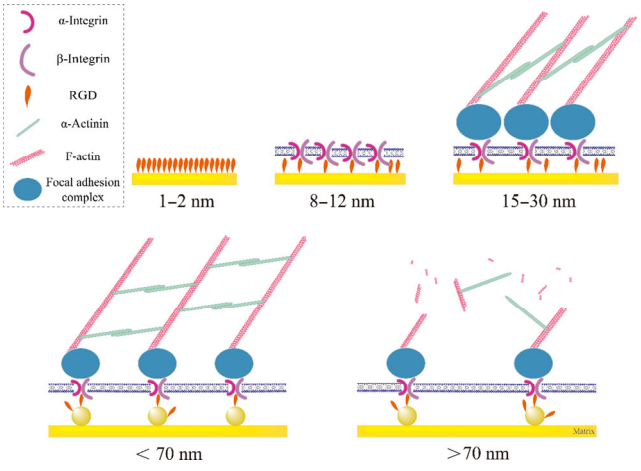

Figure 11 Schematic illustration showing the underlying RGD nanospacings to regulate cell adhesion.

gold surface with densely grafted RGDs, namely about 19 nm as shown in Fig. 7. Here, we would like to mention an elegant work from Choi and Bian groups to prepare gold nanorods and link to RGD peptides for cell studies [84]. The result of their research shows that the aspect ratios of gold nanorods could significant influence cell spreading, alignment of the basal cytoskeletal structure, and nanopodia attachment, indicating that anisotropic presentations of ligands by gold nanodots with various aspect ratios affect the activations of mechanotransduction signaling molecules. These findings demonstrate the potential to unravel the fundamental mechanisms of cell adhesion and associated signaling at the molecular level. We would like to notice that the relatively long dimensions of their nanorods and nanospheres lied between 36.5–98.2 nm, all larger than the effective RGD nanospacing of 19 nm revealed in our work. So, their hidden RGD nanospacings in nanorods must be effective along the long axes. The investigations of our nanodots and their nanorods are consistent with each other as the RGD nanospacing effect is concerned.

Figure 11 also summarizes the cellular responses of nanoarrays with RGD nanospacings larger than the "effective nanospacing," in particular, the interpretation of the "critical nanospacing" for specific cell adhesion on nanopatterns. Since the pair of α-actinin is close to 70 nm [30, 41, 85, 86], we suggest such a pair as a "nanoruler," which primarily explains the dependence of cell adhesion on RGD nanospacing, as seen in the lower row of Fig. 11.

It is worthy of indicating that Spatz group has determined that only 6 integrins with lateral spacings less than 70 nm could be sufficient to trigger an FA plaque [58]. They draw this conclusion using combination of block copolymer micelle nanolithography and e-beam lithography to fabricate a series of micro-nanopatterns. Besides the different preparation approach of their micro-nanopattern, their adjusted microislands are much smaller than the spreading area of a single cell, and called adhesive patches by them. Eventually, the Spatz group obtained a series of micro-nanopatterns of RGD peptides on nanoarrays with a lateral spacing of 58 nm and a number of gold nanoparticles of 6 nm size, ranging from 6 to 3,000 per adhesive patch. While this elegant work has determined how many integrins are involved in a single FA plaque, their publication has not concerned the critical adhesion area of cells on either micropatterns or micro-nanopatterns, possibly because the micropattern preparation using e-beam lithography is much less efficient that photolithography plus HF etching as introduced by us in combination with the block copolymer micelle lithography. What is more, the critical adhesion areas of cells on micro-nanopatterns were found to depend upon RGD nanospacing by us, and our further derivation revealed the "effective RGD nanospacing" (19 nm for the examined cell type) on micropatterns and unpatterned free surfaces with dense RGD grafting, which is not available to be investigated without the assistance of the micro-nanopatterning technique and the analysis of the critical adhesion areas. Such an effective RGD nanospacing is, to the best of our knowledge, revealed by us for the first time. Hence, an almost full hierarchal physical picture of the effects of RGD nanospacings on cell adhesion has so far been established based on the present work and also the previous efforts from Spatz's, ours and others' groups.

4.4 Background adhesion of cells on a biomaterial

In the end, we would like to emphasize that a concept of "background adhesion" is also defined in this study. It is expected to be a universal concept, which stands even in the absence of ligand–receptor binding. The mechanism of background adhesion is not clear at the moment, but it must be related to nonspecific adsorption of any mass in the cell culture media or body fluids onto material substrates and the further nonspecific cell adhesion on biomaterials, which cannot be absolutely nonfouling. The examination of its versatility and the elucidation of the underlying mechanism are strongly called for.

5 Conclusions

In the present study, we prepared a series of micro-nanopatterns with different nanospacings by combining block copolymer micelle nanolithography, photolithography, HF etching, and self-assembly monolayer. The delicate micro-nanopattern is very helpful for revealing cell–material interactions on both cellular level (microscale) and molecular level (nanoscale). We designed a series of micro-nanopatterns with varied spacings of nanodots and diameters of microislands to decouple the effects of RGD nanospacing and cell spreading size. The experimental results of hMSCs on the micro-nanopatterns confirmed a critical role of the nanoscale distribution of extracellular RGD ligands on cell adhesion. Based on series of micro-nanopatterns, we obtained critical cell adhesion areas on micro-nanopatterns for the first time and found its significant dependence upon RGD nanospacing. We deduced that the minimal effective nanospacing for cell adhesion was about 19 nm, which refers to the working RGD nanospacing on a free surface without any nanopattern yet densely grafted with RGD ligands. According to the diverse cell morphologies on micro-nanopatterns of various nanospacings and microisland sizes, we put forward the significant role of "background adhesion" for the whole cell adhesion. Eventually by combining the number of effective RGD–integrin bioconjugates and the background adhesion, we unified an almost constant adhesion content with respect to different critical adhesion areas on varied micro-nanopatterns. These fundamental investigations bring an extensive perspective of cell–material interactions on both microscale and nanoscale.

Acknowledgements

This work was financially supported by the National Key R&D Program of China (No. 2016YFC1100300) and the National Natural Science Foundation of China (Nos. 21961160721 and 21704018).

Electronic Supplementary Material: Supplementary materials

and methods (details of fabrication of micro-nanopatterns), and supplementary results (selective adhesion or localization of hMSCs on nanoarrayed microislands with non-fouling background, calculation of critical number of integrin–ligand binding N^*, etc.) are available in the online version of this article at https://doi.org/10.1007/s12274-0221-3711-6.

References

[1] Ravasio, A.; Le, A. P.; Saw, T. B.; Tarle, V.; Ong, H. T.; Bertocchi, C.; Mège, R. M.; Lim, C. T.; Gov, N. S.; Ladoux, B. Regulation of epithelial cell organization by tuning cell–substrate adhesion. *Integr. Biol.* **2015**, *7*, 1228–1241.

[2] Davidson, M. D.; Burdick, J. A.; Wells, R. G. Engineered biomaterial platforms to study fibrosis. *Adv. Healthc. Mater.* **2020**, *9*, 1901682.

[3] Salber, J.; Gräter, S.; Harwardt, M.; Hofmann, M.; Klee, D.; Dujic, J.; Jinghuan, H.; Ding, J. D.; Kippenberger, S.; Bernd, A. et al. Influence of different ECM mimetic peptide sequences embedded in a nonfouling environment on the specific adhesion of human-skin keratinocytes and fibroblasts on deformable substrates. *Small* **2007**, *3*, 1023–1031.

[4] Chen, Q.; Yu, S.; Zhang, D. H.; Zhang, W. J.; Zhang, H. D.; Zou, J. C.; Mao, Z. W.; Yuan, Y.; Gao, C. Y.; Liu, R. H. Impact of antifouling PEG layer on the performance of functional peptides in regulating cell behaviors. *J. Am. Chem. Soc.* **2019**, *141*, 16772–16780.

[5] Crosby, C. O.; Zoldan, J. Mimicking the physical cues of the ECM in angiogenic biomaterials. *Regen. Biomater.* **2019**, *6*, 61–73.

[6] Yalak, G.; Shiu, J. Y.; Schoen, I.; Mitsi, M.; Vogel, V. Phosphorylated fibronectin enhances cell attachment and upregulates mechanical cell functions. *PLoS One* **2019**, *14*, e0218893.

[7] Chen, Q.; Zhang, D. H.; Zhang, W. J.; Zhang, H. D.; Zou, J. C.; Chen, M. J.; Li, J.; Yuan, Y.; Liu, R. H. Dual mechanism β-amino acid polymers promoting cell adhesion. *Nat. Commun.* **2021**, *12*, 562.

[8] Xu, B. B.; Feng, C.; Hu, J. H.; Shi, P.; Gu, G. X.; Wang, L.; Huang, X. Y. Spin-casting polymer brush films for stimuli-responsive and anti-fouling surfaces. *ACS Appl. Mater. Interfaces* **2016**, *8*, 6685–6692.

[9] Silva, J. M.; García, J. R.; Reis, R. L.; García, A. J.; Mano, J. F. Tuning cell adhesive properties via layer-by-layer assembly of chitosan and alginate. *Acta Biomater.* **2017**, *51*, 279–293.

[10] Li, J.; Di Russo, J.; Hua, X. M.; Chu, Z. Q.; Spatz, J. P.; Wei, Q. Surface immobilized E-cadherin mimetic peptide regulates the adhesion and clustering of epithelial cells. *Adv. Healthc. Mater.* **2019**, *8*, 1801384.

[11] Gao, J. M.; Ding, X. Q.; Yu, X. Y.; Chen, X. B.; Zhang, X. Y.; Cui, S. Q.; Shi, J. Y.; Chen, J.; Yu, L.; Chen, S. et al. Cell-free bilayered porous scaffolds for osteochondral regeneration fabricated by continuous 3D-printing using nascent physical hydrogel as ink. *Adv. Healthc. Mater.* **2021**, *10*, 2001404.

[12] Xie, Y. J.; Hu, C.; Feng, Y.; Li, D. F.; Ai, T.; Huang, Y. L.; Chen, X.; Huang, L. J.; Tan, J. L. Osteoimmunomodulatory effects of biomaterial modification strategies on macrophage polarization and bone regeneration. *Regen. Biomater.* **2020**, *7*, 233–245.

[13] Chopra, A.; Kutys, M. L.; Zhang, K. H.; Polacheck, W. J.; Sheng, C. C.; Luu, R. J.; Eyckmans, J.; Hinson, J. T.; Seidman, J. G.; Seidman, C. E. et al. Force generation via β-cardiac myosin, titin, and α-actinin drives cardiac sarcomere assembly from cell-matrix adhesions. *Dev. Cell* **2018**, *44*, 87–96.e5.

[14] Doss, B. L.; Pan, M.; Gupta, M.; Grenci, G.; Mège, R. M.; Lim, C. T.; Sheetz, M. P.; Voituriez, R.; Ladoux, B. Cell response to substrate rigidity is regulated by active and passive cytoskeletal stress. *Proc. Natl. Acad. Sci. USA* **2020**, *117*, 12817–12825.

[15] Kong, F.; Li, Z. H.; Parks, W. M.; Dumbauld, D. W.; García, A. J.; Mould, A. P.; Humphries, M. J.; Zhu, C. Cyclic mechanical reinforcement of integrin–ligand interactions. *Mol. Cell* **2013**, *49*, 1060–1068.

[16] Oria, R.; Wiegand, T.; Escribano, J.; Elosegui-Artola, A.; Uriarte, J. J.; Moreno-Pulido, C.; Platzman, I.; Delcanale, P.; Albertazzi, L.; Navajas, D. et al. Force loading explains spatial sensing of ligands by cells. *Nature* **2017**, *552*, 219–224.

[17] Elloumi-Hannachi, I.; García, J. R.; Shekeran, A.; García, A. J. Contributions of the integrin β1 tail to cell adhesive forces. *Exp. Cell Res.* **2015**, *332*, 212–222.

[18] Zhou, D. W.; Lee, T. T.; Weng, S.; Fu, J. P.; García, A. J. Effects of substrate stiffness and actomyosin contractility on coupling between force transmission and vinculin-paxillin recruitment at single focal adhesions. *Mol. Biol. Cell* **2017**, *28*, 1901–1911.

[19] Yu, L. X.; Hou, Y.; Xie, W. Y.; Camacho, J. L. C.; Cheng, C.; Holle, A.; Young, J.; Trappmann, B.; Zhao, W. F.; Melzig, M. F. et al. Ligand diffusion enables force-independent cell adhesion via activating α5β1 integrin and initiating Rac and RhoA signaling. *Adv. Mater.* **2020**, *32*, 2002566.

[20] Schaufler, V.; Czichos-Medda, H.; Hirschfeld-Warnecken, V.; Neubauer, S.; Rechenmacher, F.; Medda, R.; Kessler, H.; Geiger, B.; Spatz, J. P.; Cavalcanti-Adam, E. A. Selective binding and lateral clustering of α5β1 and αvβ3 integrins: Unraveling the spatial requirements for cell spreading and focal adhesion assembly. *Cell Adhes. Migr.* **2016**, *10*, 505–515.

[21] Kechagia, J. Z.; Ivaska, J.; Roca-Cusachs, P. Integrins as biomechanical sensors of the microenvironment. *Nat. Rev. Mol. Cell Biol.* **2019**, *20*, 457–473.

[22] Sales, A.; Ende, K.; Diemer, J.; Kyvik, A. R.; Veciana, J.; Ratera, I.; Kemkemer, R.; Spatz, J. P.; Guasch, J. Cell type-dependent integrin distribution in adhesion and migration responses on protein-coated microgrooved substrates. *ACS Omega* **2019**, *4*, 1791–1800.

[23] Liu, Q.; Zheng, S.; Ye, K.; He, J. H.; Shen, Y.; Cui, S. Q.; Huang, J. L.; Gu, Y. X.; Ding, J. D. Cell migration regulated by RGD nanospacing and enhanced under moderate cell adhesion on biomaterials. *Biomaterials* **2020**, *263*, 120327.

[24] Kang, H.; Wong, D. S. H.; Yan, X. H.; Jung, H. J.; Kim, S.; Lin, S.; Wei, K. C.; Li, G.; Dravid, V. P.; Bian, L. M. Remote control of multimodal nanoscale ligand oscillations regulates stem cell adhesion and differentiation. *ACS Nano* **2017**, *11*, 9636–9649.

[25] Pallarola, D.; Platzman, I.; Bochen, A.; Cavalcanti-Adam, E. A.; Axmann, M.; Kessler, H.; Geiger, B.; Spatz, J. P. Focal adhesion stabilization by enhanced integrin-*c*RGD binding affinity. *BioNanoMaterials* **2017**, *18*, 20160014.

[26] Li, J. C.; Chen, Y.; Kawazoe, N.; Chen, G. P. Ligand density-dependent influence of arginine–glycine–aspartate functionalized gold nanoparticles on osteogenic and adipogenic differentiation of mesenchymal stem cells. *Nano Res.* **2018**, *11*, 1247–1261.

[27] Kafi, M. A.; Aktar, K.; Todo, M.; Dahiya, R. Engineered chitosan for improved 3D tissue growth through Paxillin-FAK-ERK activation. *Regen. Biomater.* **2020**, *7*, 141–151.

[28] Wong, S. H. D.; Wong, W. K. R.; Lai, C. H. N.; Oh, J.; Li, Z.; Chen, X. Y.; Yuan, W. H.; Bian, L. M. Soft polymeric matrix as a macroscopic cage for magnetically modulating reversible nanoscale ligand presentation. *Nano Lett.* **2020**, *20*, 3207–3216.

[29] Massia, S. P.; Hubbell, J. A. An RGD spacing of 440 nm is sufficient for integrin alpha V beta 3-mediated fibroblast spreading and 140 nm for focal contact and stress fiber formation. *J. Cell Biol.* **1991**, *114*, 1089–1100.

[30] Cavalcanti-Adam, E. A.; Volberg, T.; Micoulet, A.; Kessler, H.; Geiger, B.; Spatz, J. P. Cell spreading and focal adhesion dynamics are regulated by spacing of integrin ligands. *Biophys. J.* **2007**, *92*, 2964–2974.

[31] Graeter, S. V.; Huang, J.; Perschmann, N.; López-García, M.; Kessler, H.; Ding, J. D.; Spatz, J. P. Mimicking cellular environments by nanostructured soft interfaces. *Nano Lett.* **2007**, *7*, 1413–1418.

[32] Cheng, Z. A.; Zouani, O. F.; Glinel, K.; Jonas, A. M.; Durrieu, M. C. Bioactive chemical nanopatterns impact human mesenchymal stem cell fate. *Nano Lett.* **2013**, *13*, 3923–3929.

[33] Lagunas, A.; Castaño, A. G.; Artés, J. M.; Vida, Y.; Collado, D.; Pérez-Inestrosa, E.; Gorostiza, P.; Claros, S.; Andrades, J. A.; Samitier, J. Large-scale dendrimer-based uneven nanopatterns for the study of local arginine–glycine–aspartic acid (RGD) density effects on cell adhesion. *Nano Res* **2014**, *7*, 399–409.

[34] Tsimbouri, P.; Gadegaard, N.; Burgess, K.; White, K.; Reynolds, P.; Herzyk, P.; Oreffo, R.; Dalby, M. J. Nanotopographical effects on mesenchymal stem cell morphology and phenotype. *J. Cell. Biochem.* **2014**, *115*, 380–390.

[35] Li, S. Y.; Wang, X.; Cao, B.; Ye, K.; Li, Z. H.; Ding, J. D. Effects of nanoscale spatial arrangement of arginine–glycine–aspartate peptides on dedifferentiation of chondrocytes. *Nano Lett.* **2015**, *15*, 7755–7765.

[36] Mashinchian, O.; Turner, L. A.; Dalby, M. J.; Laurent, S.; Shokrgozar, M. A.; Bonakdar, S.; Imani, M.; Mahmoudi, M. Regulation of stem cell fate by nanomaterial substrates. *Nanomedicine* **2015**, *10*, 829–847.
[37] Ye, K.; Cao, L. P.; Li, S. Y.; Yu, L.; Ding, J. D. Interplay of matrix stiffness and cell–cell contact in regulating differentiation of stem cells. *ACS Appl. Mater. Interfaces* **2016**, *8*, 21903–21913.
[38] Lagunas, A.; Tsintzou, I.; Vida, Y.; Collado, D.; Pérez-Inestrosa, E.; Pereira, C. R.; Magalhaes, J.; Andrades, J. A.; Samitier, J. Tailoring RGD local surface density at the nanoscale toward adult stem cell chondrogenic commitment. *Nano Res.* **2017**, *10*, 1959–1971.
[39] Zhang, M.; Sun, Q.; Liu, Y. L.; Chu, Z. Q.; Yu, L. X.; Hou, Y.; Kang, H.; Wei, Q.; Zhao, W. F.; Spatz, J. P. et al. Controllable ligand spacing stimulates cellular mechanotransduction and promotes stem cell osteogenic differentiation on soft hydrogels. *Biomaterials* **2021**, *268*, 120543.
[40] Arnold, M.; Cavalcanti-Adam, E. A.; Glass, R.; Blümmel, J.; Eck, W.; Kantlehner, M.; Kessler, H.; Spatz, J. P. Activation of integrin function by nanopatterned adhesive interfaces. *ChemPhysChem* **2004**, *5*, 383–388.
[41] Huang, J. H.; Gräter, S. V.; Corbellini, F.; Rinck, S.; Bock, E.; Kemkemer, R.; Kessler, H.; Ding, J. D.; Spatz, J. P. Impact of order and disorder in RGD nanopatterns on cell adhesion. *Nano Lett.* **2009**, *9*, 1111–1116.
[42] Liu, Y.; Medda, R.; Liu, Z.; Galior, K.; Yehl, K.; Spatz, J. P.; Cavalcanti-Adam, E. A.; Salaita, K. Nanoparticle tension probes patterned at the nanoscale: Impact of integrin clustering on force transmission. *Nano Lett.* **2014**, *14*, 5539–5546.
[43] Ye, K.; Wang, X.; Cao, L. P.; Li, S. Y.; Li, Z. H.; Yu, L.; Ding, J. D. Matrix stiffness and nanoscale spatial organization of cell-adhesive ligands direct stem cell fate. *Nano Lett.* **2015**, *15*, 4720–4729.
[44] Deng, J.; Zhao, C. S.; Spatz, J. P.; Wei, Q. Nanopatterned adhesive, stretchable hydrogel to control ligand spacing and regulate cell spreading and migration. *ACS Nano* **2017**, *11*, 8282–8291.
[45] Gallant, N. D.; Capadona, J. R.; Frazier, A. B.; Collard, D. M.; García, A. J. Micropatterned surfaces to engineer focal adhesions for analysis of cell adhesion strengthening. *Langmuir* **2002**, *18*, 5579–5584.
[46] Yao, X.; Peng, R.; Ding, J. D. Cell–material interactions revealed via material techniques of surface patterning. *Adv. Mater.* **2013**, *25*, 5257–5286.
[47] Estévez, M.; Martínez, E.; Yarwood, S. J.; Dalby, M. J.; Samitier, J. Adhesion and migration of cells responding to microtopography. *J. Biomed. Mater. Res.* **2015**, *103*, 1659–1668.
[48] Sonam, S.; Sathe, S. R.; Yim, E. K. F.; Sheetz, M. P.; Lim, C. T. Cell contractility arising from topography and shear flow determines human mesenchymal stem cell fate. *Sci. Rep.* **2016**, *6*, 20415.
[49] Cao, B.; Peng, Y. M.; Liu, X. N.; Ding, J. D. Effects of functional groups of materials on nonspecific adhesion and chondrogenic induction of mesenchymal stem cells on free and micropatterned surfaces. *ACS Appl. Mater. Interfaces* **2017**, *9*, 23574–23585.
[50] Cho, D. H.; Xie, T.; Truong, J.; Stoner, A. C.; Hahm, J. I. Recent advances towards single biomolecule level understanding of protein adsorption phenomena unique to nanoscale polymer surfaces with chemical variations. *Nano Res.* **2020**, *13*, 1295–1317.
[51] Liu, R. L.; Ding, J. D. Chromosomal repositioning and gene regulation of cells on a micropillar array. *ACS Appl. Mater. Interfaces* **2020**, *12*, 35799–35812.
[52] Yao, X.; Ding, J. D. Effects of microstripe geometry on guided cell migration. *ACS Appl. Mater. Interfaces* **2020**, *12*, 27971–27983.
[53] Zhao, P.; Li, X.; Fang, Q.; Wang, F. L.; Ao, Q.; Wang, X. H.; Tian, X. H.; Tong, H.; Bai, S. L.; Fan, J. Surface modification of small intestine submucosa in tissue engineering. *Regen. Biomater.* **2020**, *7*, 339–348.
[54] Yao, X.; Wang, X. L.; Ding, J. D. Exploration of possible cell chirality using material techniques of surface patterning. *Acta Biomater.* **2021**, *126*, 92–108.
[55] Chen, C. S.; Mrksich, M.; Huang, S.; Whitesides, G. M.; Ingber, D. E. Geometric control of cell life and death. *Science* **1997**, *276*, 1425–1428.
[56] Yan, C.; Sun, J. G.; Ding, J. D. Critical areas of cell adhesion on micropatterned surfaces. *Biomaterials* **2011**, *32*, 3931–3938.
[57] Glass, R.; Möller, M.; Spatz, J. P. Block copolymer micelle nanolithography. *Nanotechnology* **2003**, *14*, 1153–1160.
[58] Arnold, M.; Schwieder, M.; Blümmel, J.; Cavalcanti-Adam, E. A.; López-Garcia, M.; Kessler, H.; Geiger, B. et al. Cell interactions with hierarchically structured nano-patterned adhesive surfaces. *Soft Matter* **2009**, *5*, 72–77.
[59] Wang, X.; Li, S. Y.; Yan, C.; Liu, P.; Ding, J. D. Fabrication of RGD micro/nanopattern and corresponding study of stem cell sifferentiation. *Nano Lett.* **2015**, *15*, 1457–1467.
[60] Wang, L. Y.; Cai, P. Q.; Luo, J.; Zhang, F. L.; Liu, J.; Chen, Y. P.; Zhu, Z. P.; Song, Y. Y.; Yang, B. Q.; Liu, X. et al. Engineering subcellular-patterned biointerfaces to regulate the surface wetting of multicellular spheroids. *Nano Res.* **2018**, *11*, 5704–5715.
[61] Dai, J.; Yao, Y. Adaptive ordering and filament polymerization of cell cytoskeleton by tunable nanoarrays. *Nano Res.* **2021**, *14*, 620–627.
[62] Yao, X.; Liu, R. L.; Liang, X. Y.; Ding, J. D. Critical areas of proliferation of single cells on micropatterned surfaces and corresponding cell type dependence. *ACS Appl. Mater. Interfaces* **2019**, *11*, 15366–15380.
[63] Xiong, J. P.; Stehle, T.; Diefenbach, B.; Zhang, R. G.; Dunker, R.; Scott, D. L.; Joachimiak, A.; Goodman, S. L.; Arnaout, M. A. Crystal structure of the extracellular segment of integrin αVβ3. *Science* **2001**, *294*, 339–345.
[64] Xiong, J. P.; Stehle, T.; Zhang, R. G.; Joachimiak, A.; Frech, M.; Goodman, S. L.; Arnaout, M. A. Crystal structure of the extracellular segment of integrin αVβ3 in complex with an Arg-Gly-Asp ligand. *Science* **2002**, *296*, 151–155.
[65] Jiang, Y. H.; Jahagirdar, B. N.; Reinhardt, R. L.; Schwartz, R. E.; Keene, C. D.; Ortiz-Gonzalez, X. R.; Reyes, M.; Lenvik, T.; Lund, T.; Blackstad, M. et al. Pluripotency of mesenchymal stem cells derived from adult marrow. *Nature* **2002**, *418*, 41–49.
[66] Even-Ram, S.; Artym, V.; Yamada, K. M. Matrix control of stem cell fate. *Cell* **2006**, *126*, 645–647.
[67] Peng, R.; Yao, X.; Ding, J. D. Effect of cell anisotropy on differentiation of stem cells on micropatterned surfaces through the controlled single cell adhesion. *Biomaterials* **2011**, *32*, 8048–8057.
[68] Peng, Y. M.; Liu, Q. J.; He, T. L.; Ye, K.; Yao, X.; Ding, J. D. Degradation rate affords a dynamic cue to regulate stem cells beyond varied matrix stiffness. *Biomaterials* **2018**, *178*, 467–480.
[69] Saburi, E.; Abazari, M. F.; Hassannia, H.; Mansour, R. N.; Eshaghi-Gorji, R.; Gheibi, M.; Rahmati, M.; Enderami, S. E. The use of mesenchymal stem cells in the process of treatment and tissue regeneration after recovery in patients with Covid-19. *Gene* **2021**, *777*, 145471.
[70] Mao, T. J.; He, Y. N.; Gu, Y. X.; Yang, Y. Q.; Yu, Y.; Wang, X. L.; Ding, J. D. Critical frequency and critical stretching rate for reorientation of cells on a cyclically stretched polymer in a microfluidic chip. *ACS Appl. Mater. Interfaces* **2021**, *13*, 13934–13948.
[71] Haubner, R.; Gratias, R.; Diefenbach, B.; Goodman, S. L.; Jonczyk, A.; Kessler, H. Structural and functional aspects of RGD-containing cyclic pentapeptides as highly potent and selective integrin $\alpha v\beta_3$ antagonists. *J. Am. Chem. Soc.* **1996**, *118*, 7461–7472.
[72] Hersel, U.; Dahmen, C.; Kessler, H. RGD modified polymers: Biomaterials for stimulated cell adhesion and beyond. *Biomaterials* **2003**, *24*, 4385–4415.
[73] Cui, S. Q.; Yu, L.; Ding, J. D. Strategy of "Block Blends" to generate polymeric thermogels versus that of one-component block copolymer. *Macromolecules* **2020**, *53*, 11051–11064.
[74] Cui, S. Q.; Chen, L.; Yu, L.; Ding, J. D. Synergism among polydispersed amphiphilic block copolymers leading to spontaneous physical hydrogelation upon heating. *Macromolecules* **2020**, *53*, 7726–7739.
[75] Lehnert, D.; Wehrle-Haller, B.; David, C.; Weiland, U.; Ballestrem, C.; Imhof, B. A.; Bastmeyer, M. Cell behaviour on micropatterned substrata: Limits of extracellular matrix geometry for spreading and adhesion. *J. Cell Sci.* **2004**, *117*, 41–52.
[76] Gallant, N. D.; Michael, K. E.; García, A. J. Cell adhesion strengthening: Contributions of adhesive area, integrin binding, and focal adhesion assembly. *Mol. Biol. Cell* **2005**, *16*, 4329–4340.
[77] Coyer, S. R.; Singh, A.; Dumbauld, D. W.; Calderwood, D. A.;

Craig, S. W.; Delamarche, E.; García, A. J. Nanopatterning reveals an ECM area threshold for focal adhesion assembly and force transmission that is regulated by integrin activation and cytoskeleton tension. *J. Cell Sci*. **2012**, *125*, 5110–5123.

[78] Wang, R.; Lin, T. S.; Johnson, J. A.; Olsen, B. D. Kinetic monte carlo simulation for quantification of the gel point of polymer networks. *ACS Marco Lett*. **2017**, *6*, 1414–1419.

[79] Guo, M.; Pegoraro, A. F.; Mao, A.; Zhou, E. H.; Arany, P. R.; Han, Y. L.; Burnette, D. T.; Jensen, M. H.; Kasza, K. E.; Moore, J. R. et al. Cell volume changethrough water efflux impacts cell stiffness and stem cell fate. *Proc*. *Natl*. *Acad*. *Sci*. *USA* **2017**, *114*, E8618–E8627.

[80] Chen, C. S.; Alonso, J. L.; Ostuni, E.; Whitesides, G. M.; Ingber, D. E. Cell shape provides global control of focal adhesion assembly. *Biochem*. *Biophys*. *Res*. *Commun*. **2003**, *307*, 355–361.

[81] Jiun, K.; Hong, S. Y.; Park, H. S.; Kim, D. S.; Lee, W. Structure and function of RGD peptides derived from disintegrin proteins. *Mol*. *Cells* **2005**, *19*, 205–211.

[82] Takagi, J.; Petre, B. M.; Walz, T.; Springer, T. A. Global conformational rearrangements in integrin extracellular domains in outside-in and inside-out signaling. *Cell* **2002**, *110*, 599–611.

[83] Craig, D.; Gao, M.; Schulten, K.; Vogel, V. Structural insights into how the MIDAS ion stabilizes integrin binding to an RGD peptide under force. *Structure* **2004**, *12*, 2049–2058.

[84] Wong, S. H. D.; Yin, B. H.; Yang, B. G.; Lin, S. E.; Li, R.; Feng, Q.; Yang, H. R.; Zhang, L.; Yang, Z. M.; Li, G. et al. Anisotropic nanoscale presentation of cell adhesion ligand enhances the recruitment of diverse integrins in adhesion structures and mechanosensing-dependent differentiation of stem cells. *Adv*. *Funct*. *Mater*. **2019**, *29*, 1806822.

[85] Meyer, R. K.; Aebi, U. Bundling of actin filaments by α-Actinin depends on its molecular length. *J*. *Cell Biol*. **1990**, *110*, 2013–2024.

[86] Arnold, M.; Hirschfeld-Warneken, V. C.; Lohmüller, T.; Heil, P.; Blümmel, J.; Cavalcanti-Adam, E. A.; López-García, M.; Walther, P.; Kessler, H.; Geiger, B. et al. Induction of cell polarization and migration by a gradient of nanoscale variations in adhesive ligand spacing. *Nano Lett*. **2008**, *8*, 2063–2069.